

Design of a high sensitivity and wide range angular rate sensor based on exceptional surface

Xinsheng Ding(丁鑫圣), Wenyao Liu(刘文耀), Shixian Wang(王师贤), Yu Tao(陶煜), Yanru Zhou(周彦汝), Yu Bai(白禹), Lai Liu(刘来), Enbo Xing(邢恩博), Jun Tang(唐军), and Jun Liu(刘俊)
Citation: Chin. Phys. B, 2024, 33 (**8**): 084204. DOI: 10.1088/1674-1056/ad4324

What follows is a list of articles you may be interested in

Design of compact integrated diamond nitrogen-vacancy center quantum probe

Sheng-Kai Xia(夏圣开), Wen-Tao Lu(卢文韬), Xu-Tong Zhao(赵旭彤), Ya-Wen Xue(薛雅文), Zeng-Bo Xu(许增博), Shi-Yu Ge(葛仕宇), Yang Wang(汪洋), Lin-Yan Yu(虞林嫣), Yu-Chen Bian(卞雨辰), Si-Han An(安思瀚), Bo Yang(杨博), Jian-Jun Xiang(向建军), and Guan-Xiang Du(杜关祥)
Chin. Phys. B, 2024, 33 (**5**): 054202. DOI: 10.1088/1674-1056/ad2bf6

Engineered photonic spin Hall effect of Gaussian beam in antisymmetric parity-time metamaterials

Lu-Yao Liu(刘露遥), Zhen-Xiao Feng(冯振校), Dong-Mei Deng(邓冬梅), and Guang-Hui Wang(王光辉)
Chin. Phys. B, 2023, 32 (**9**): 094201. DOI: 10.1088/1674-1056/accb89

Anti-$\mathcal{PT}$-symmetric Kerr gyroscope

Huilai Zhang(张会来), Meiyu Peng(彭美瑜), Xun-Wei Xu(徐勋卫), and Hui Jing(景辉)
Chin. Phys. B, 2022, 31 (**1**): 014215. DOI: 10.1088/1674-1056/ac3988

Fabry-Pérot resonance coupling associated exceptional points in a composite grating structure

Zhi-Sen Jiang(蒋之森), De-Jiao Hu(胡德娇), Lin Pang(庞霖), Fu-Hua Gao(高福华), Ping Wang(王平)
Chin. Phys. B, 2018, 27 (**5**): 054201. DOI: 10.1088/1674-1056/27/5/054201

Bifurcated overtones of one-way localized Fabry–Pérot resonances in parity-time symmetric optical lattices

Fatma Nafaa Gaafer, Yaxi Shen(沈亚西), Yugui Peng(彭玉桂), Aimin Wu(武爱民), Peng Zhang(张鹏), Xuefeng Zhu(祝雪丰)
Chin. Phys. B, 2017, 26 (**7**): 074218. DOI: 10.1088/1674-1056/26/7/074218

Design of a high sensitivity and wide range angular rate sensor based on exceptional surface

Xinsheng Ding(丁鑫圣)[1], Wenyao Liu(刘文耀)[1,2,†], Shixian Wang(王师贤)[1], Yu Tao(陶煜)[1], Yanru Zhou(周彦汝)[1,2], Yu Bai(白禹)[1,2], Lai Liu(刘来)[1,2], Enbo Xing(邢恩博)[1,2], Jun Tang(唐军)[1,2,‡], and Jun Liu(刘俊)[1,2,§]

[1] *State Key Laboratory of Dynamic Measurement Technology, North University of China, Taiyuan* 030051, *China*
[2] *Shanxi Province Key Laboratory of Quantum Sensing and Precision Measurement, North University of China, Taiyuan* 030051, *China*

(Received 21 November 2023; revised manuscript received 24 April 2024; accepted manuscript online 25 April 2024)

It is found that when the parity–time symmetry phenomenon is introduced into the resonant optical gyro system and it works near the exceptional point, the sensitivity can in theory be significantly amplified at low angular rate. However, in fact, the exceptional point is easily disturbed by external environmental variables, which means that it depends on harsh experimental environment and strong control ability, so it is difficult to move towards practical application. Here, we propose a new angular rate sensor structure based on exceptional surface, which has the advantages of high sensitivity and high robustness. The system consists of two fiber-optic ring resonators and two optical loop mirrors, and one of the resonators contains a variable ratio coupler and a variable optical attenuator. We theoretically analyze the system response, and the effects of phase and coupling ratio on the system response. Finally, compared with the conventional resonant gyro, the sensitivity of this exceptional surface angular rate sensor can be improved by about 300 times at low speed. In addition, by changing the loss coefficient in the ring resonator, we can achieve a wide range of 600 rad/s. This scheme provides a new approach for the development of ultra-high sensitivity and wide range angular rate sensors in the future.

Keywords: exceptional surface, exceptional points, ring resonator, angular rate sensing, rotational direction recognition, wide operating range

PACS: 42.81.Pa, 42.81.Qb **DOI:** 10.1088/1674-1056/ad4324

1. Introduction

Conventional resonant gyroscopes mainly rely on the Sagnac effect to detect rotation angular rate. Rotation causes an optical path difference between the clockwise (CW) and counterclockwise (CCW) directions. The difference between the clockwise resonant frequency and the counterclockwise resonant frequency of the ring resonator is equal to the rotation angular rate is a linear function.[1] But this also means that when the angular rate of rotation is low, the frequency difference is also quite small. According to the formula, 0.1 °/h causes an equivalent change of 10^{-17} cm for a ring resonator with a radius of 1 cm. Such a small response may even be submerged in external interference, making it difficult to distinguish. The conventional solution is to suppress noise and increase the size of the ring resonator,[2] which makes it difficult for the resonant gyroscope to combine the advantages of volume and accuracy.[3]

In recent years, some research teams have gradually made up for the disadvantages of resonant gyroscopes at low speeds by placing the sensor operating point near the exceptional point (EP).[4–8] A common one is the parity–time (PT)-symmetric system,[9,10] which constructs a critical EP between the PT-symmetric phase and the PT-damaged phase by adjusting the gain–loss coupling ring resonator. An EP represents the fusion of two eigenvalues and eigenvectors. The sensitivity is extremely high near the EP,[11] and the system response $\Delta\omega_{\mathrm{PT}} \sim 2\sqrt{\Delta\omega\kappa}$.[10] Compared with linear systems, PT systems respond more prominently to frequency perturbations, but such responses are reflected in the broadening of the transmission spectrum, and both gain and loss need to be carefully controlled.[12,13] In order to reduce the measurement error and reduce the difficulty of system control, de Carlo proposed to introduce the anti-parity time symmetry structure into the optical gyroscope.[14] When the system is subject to frequency perturbations, the system response manifests itself as frequency splitting.[15–18] The most representative is Vahala used an on-chip non-Hermitian Brillouin gyroscope to collect the Earth's rotation angular rate. The angular random walk reached 0.068 °$\mathrm{h}^{-1/2}$, proving that a gyroscope working near an EP can achieve both volume and accuracy advantage.[19,20] However, in practical applications, although the EP gyroscope can display extremely high sensitivity, its operating point is also very sensitive to disturbances from non-measurement factors. Small manufacturing tolerances and external disturbances can cause undesirable shifts in the operating point and greatly reduce sensitivity.[21–23]

†Corresponding author. E-mail: liuwenyao@nuc.edu.cn
‡Corresponding author. E-mail: tangjun@nuc.edu.cn
§Corresponding author. E-mail: liuj@nuc.edu.cn

© 2024 Chinese Physical Society and IOP Publishing Ltd

Therefore, Zhong *et al*. at Michigan Technological University proposed the concept of exceptional surfaces (ES) and gave a single-cavity structure with added particles and mirrors.[24] The measurement of particle size can coexist with high sensitivity and robustness. ES are composed of countless EPs, providing additional degrees of freedom. This allows the system operating point to wander on the exceptional surface under the influence of manufacturing tolerances and undesired external disturbances, ensuring that the operating point falls stably on the exceptional point in a non-rotating state. When the system is subject to a disturbance to be measured, the disturbance to be measured pushes the operating point away from the ES and generates a huge response. The sensitivity is still considerable within the small disturbance range.[25] Subsequently, Ş. K. Özdemir used experiments to prove the chirality and perfect absorption of ES in a common single-cavity structure with a fiber optical mirror added.[26] Long added particles and a mirror to the single-cavity structure and replaced the mirror with a ring-shaped optical fiber to achieve unidirectional coupling control of the clockwise mode and the counterclockwise mode.[25] In subsequent improvements, he proposed a third-order exceptional surface, this structure can also be extended to an N-order exceptional surface.[27] Xiao achieved high-sensitivity angular rate detection by adding a π phase-shift grating and using ES in a single microcavity structure with a mirror.[28] However, we found that in related research, angular rate measurement with ES cannot determine the direction, and it is difficult to balance wide range and high accuracy.

In this paper, we add a reflection device composed of a fiber loop mirror and a critical coupling ring resonator to the classic exceptional surface structure, thereby realizing the frequency perturbation response caused by the rotation through the exceptional surface, making it both sensitive and robust. At the same time, our structure supports high-sensitivity operation over a wide range.

In Section 2, we will introduce our structure in detail and the relationship between ES and angular rate sensing. In Section 3, we will analyze the relationship between the system's response and some key adjustable parameters. In Section 4, we will introduce how our exceptional surface angular rate sensor realizes range transformation and detection of rotation direction.

2. Model

A common structure for ES is a ring resonator coupled to an optical fiber with a mirror at the end, and ours is no exception. In order for the structure to work on the exceptional surface, the one-way coupling from mode 1 to mode 2 needs to be guaranteed, but the coupling from mode 2 to mode 1 needs to be completely suppressed. Such a relationship can be represented by a Hamilton matrix

$$H_{\mathrm{ES}} = \begin{bmatrix} \omega_0 - \mathrm{i}\Gamma & 0 \\ \kappa_{12} & \omega_0 - \mathrm{i}\Gamma \end{bmatrix}. \tag{1}$$

The eigenfrequency is obtained by $\omega_{\mathrm{ES}} = \omega_0 - \mathrm{i}\Gamma$. It can be seen that when the one-way coupling from mode 2 to mode 1 is strictly suppressed, the coupling rate from mode 1 to mode 2 does not change the characteristic frequency. In this case, when the frequency perturbation ε caused by rotation

$$H_{\mathrm{ES}} = \begin{bmatrix} \omega_0 + \varepsilon - \mathrm{i}\Gamma & 0 \\ \kappa_{12} & \omega_0 - \varepsilon - \mathrm{i}\Gamma \end{bmatrix}. \tag{2}$$

The eigenfrequencies are calculated and the difference between the two eigenfrequencies is $\Delta\omega = 2\varepsilon$, which shows the strong linearity similar to the conventional resonator gyroscope with single whispering gallery mode structure, and does not get the square-root dependence we want, but when the unidirectional coupling rate from mode 2 to mode 1 is changed by $\Delta\kappa_{21}$, its Hamiltonian matrix can be obtained as

$$H_{\mathrm{EP}} = \begin{bmatrix} \omega_0 - \mathrm{i}\Gamma & \Delta\kappa_{21} \\ \kappa_{12} & \omega_0 - \mathrm{i}\Gamma \end{bmatrix}. \tag{3}$$

Then we find the eigenfrequency of the matrix and obtain the relationship $\omega_{\mathrm{EP}} = \omega_0 - \mathrm{i}\Gamma \pm \sqrt{\kappa_{12}\Delta\kappa_{21}}$. If the unidirectional coupling rate from mode 1 to mode 2 is constant, it is obvious that the splitting trajectory is square root dependent, so the angular rate must be directly related to the unidirectional coupling rate from mode 2 to mode 1 without the angular rate affecting the unidirectional coupling rate from mode 1 to mode 2 too much. Based on this, the angular rate sensing enhancement structure we proposed based on ES is shown in Fig. 1, which can be roughly divided into two parts: the exceptional surface structure and the additional reflection structure.

For the structure of the exceptional surface, we still use the classic single-cavity structure, which is achieved by coupling the ring resonator RS to an optical fiber with an optical loop mirror at the end. The optical loop mirror is a very simple, reliable and variable reflectivity semi-transparent mirror. It is composed of two port pigtails on one side of a 2×2 directional fiber coupler connected together. Neglecting the loss, its ideal reflectivity r_{M} is determined by the coupler power separation ratio[29,30]

$$r_{\mathrm{M}} = \sqrt{4C_\kappa(1-C_\kappa)}, \tag{4}$$

where C_κ is the coupling power ratio and the transmission power ratio is $1-C_\kappa$. In the ES structure, the optical loop reflector can not only reflect the clockwise mode of the resonator RS to the counterclockwise mode with reflectivity r_{R} but also transmit a part of the light to the light output end a_{out} with transmissivity $\sqrt{1-r_{\mathrm{R}}^2}$.

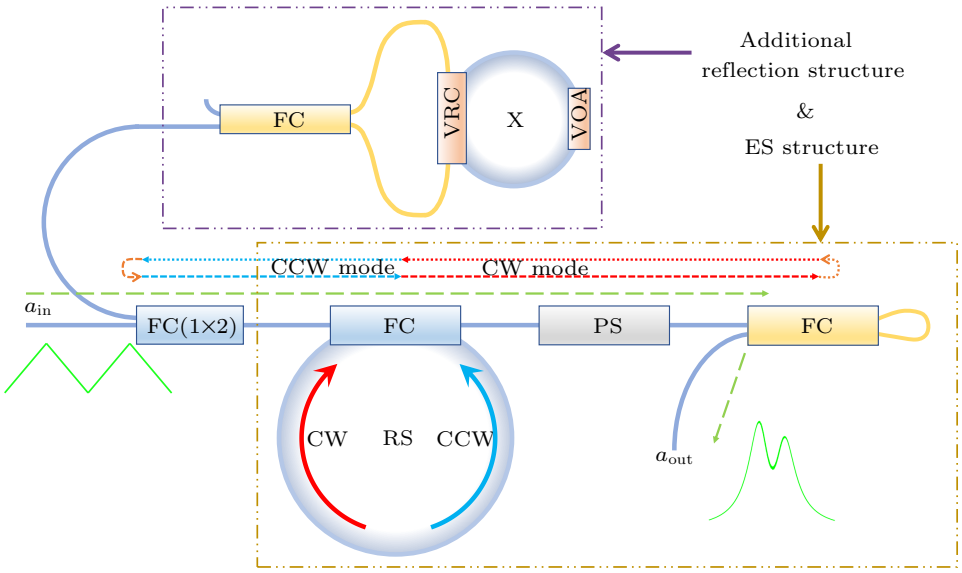


Fig. 1. Structure diagram of angular rate sensor with exceptional surface. FC: fiber coupler. PS: phase shifter. RS: rotation-sensitive resonator. X: resonator X. VRC: variable ratio coupler. VOA: variable optical attenuator.

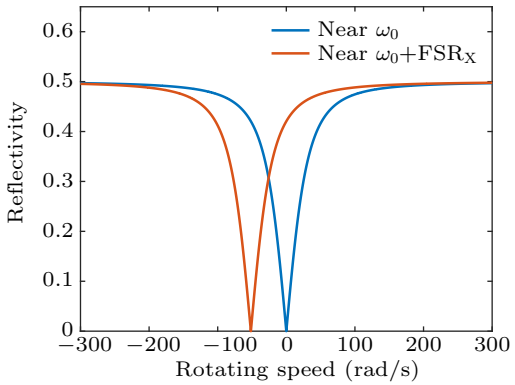


Fig. 2. The relationship between the reflectivity of the variable reflectivity device group at the resonant frequency of the rotation-sensitive ring resonator and the rotation angular rate. In the figure we use the parameter $\alpha = 0.98$. The FC power separation ratio in both the left and right fiber loop mirrors is 85:15. The power separation ratio of FC(1×2) is 50:50. The area of the resonator RS is 0.0225 m^2 and the area of the resonator X is 0.011166 m^2.

The additional reflection structure is composed of a resonator X critically coupled to the fiber loop mirror, and its function is to reflect the counterclockwise mode of the resonator RS to the clockwise mode. In order to facilitate the control of the critical coupling state and subsequent research, we used variable ratio couplers and variable optical attenuators. It is worth mentioning that our optical fiber ring resonator X uses half clockwise winding and half counterclockwise winding. This makes the area and number of circles enclosed in the clockwise direction equal to the area and number of circles enclosed in the counterclockwise direction. According to the Sagnac effect, the clockwise optical path change of such a structure will offset the counterclockwise optical path change in a rotating environment, so that the resonant frequency center will not shift in frequency with rotation in both directions. On this basis, we can obtain the relationship between the working phase and the reflection structure (see Section 4 for detailed derivation). Since our CCW mode is generated by the resonator RS, we can get the relationship between the rotation angular rate and the reflectivity r_L at the CCW mode resonant frequency as shown in Fig. 2. It is worth mentioning that the reflectivity r_L includes the beam splitting ratio of the 1×2 coupler, and the frequency shift of the modes is much smaller than the interference frequency period caused by the 1×2 coupler.

The output wavelength of the laser at a_{in} varies linearly under the voltage signal of the triangle wave, and the photodetector is connected at the position of a_{out}, so that the transmission spectrum can be output to the photodetector completely. When the light is input from a_{in}, part of it goes into the resonator to produce a clockwise mode, and part of it goes into the optical loop mirror to be reflected back into the resonator to produce a counterclockwise mode. At the same time, the unidirectional coupling from the clockwise mode to the counterclockwise mode is realized. The light then enters the variable reflectivity device group, and then bounces back into the ring resonator according to the reflectivity r_L of the corresponding frequency, this realizes the unidirectional coupling from counterclockwise mode to clockwise mode, according to which we can list the coupled mode equations

$$\mathrm{i}\frac{\mathrm{d}a_{CW}}{\mathrm{d}t} = (\Delta - \mathrm{i}\Gamma)a_{CW} + \kappa_1 a_{CCW} - \mathrm{i}\sqrt{\kappa}\,\mathrm{e}^{\mathrm{i}\theta_1}a_{in}, \quad (5)$$

$$\mathrm{i}\frac{\mathrm{d}a_{CCW}}{\mathrm{d}t} = (\Delta - \mathrm{i}\Gamma)a_{CCW} + \kappa_2 a_{CW} - \mathrm{i}r_R\sqrt{\kappa}\,\mathrm{e}^{\mathrm{i}(\theta_1+2\theta_2)}a_{in}, \quad (6)$$

where a_{in} is the input signal and θ_1 is the phase difference between the coupler of the intermediate resonator RS and the additional reflection structure, θ_2 is the phase difference between the coupler of the intermediate resonator RS and the right optical loop mirror. $\kappa_1 = r_L(\omega_{CCW})\,\mathrm{e}^{2\mathrm{i}\theta_1}\kappa$, $\kappa_2 = r_R\,\mathrm{e}^{2\mathrm{i}\theta_2}\kappa$, $\Delta = \omega_s - \omega_0$, ω_s means scan frequency, ω_0 is the reference frequency of clockwise and counterclockwise modes when the ring resonator rotates at 0. Accordingly, we can list the Hamil-

tonian matrix of the system

$$H_{\text{eff}} = \begin{bmatrix} \omega_0 - \mathrm{i}\Gamma & \kappa_1(\omega_{\text{CCW}}) \\ \kappa_2 & \omega_0 - \mathrm{i}\Gamma \end{bmatrix}. \tag{7}$$

Obviously κ_2 is a non-zero value. In order to form an exceptional surface, we need to make $\kappa_1 = 0$ at the reference frequency ω_0. We can use the piezoelectric ceramic in the resonator X to add axial stress to the resonator X by adjusting the driving voltage applied to the piezoelectric ceramic, so that the resonant frequency center of resonator X coincides with the reference frequency. Now ω_0 also refers to the frequency at which the resonant frequencies of ring resonator X and the ring resonator RS coincide. The counterclockwise mode cannot be coupled to the clockwise mode because the reflectivity is 0. The system Hamiltonian is

$$H_{\text{ES}} = \begin{bmatrix} \omega_0 - \mathrm{i}\Gamma & 0 \\ \kappa_2 & \omega_0 - \mathrm{i}\Gamma \end{bmatrix}. \tag{8}$$

Let $\det(H_{\text{ES}} - \omega_{\text{ES}}E) = 0$, we can get the characteristic frequency of $\omega_{\text{ES}} = \omega_0 - \mathrm{i}\Gamma$, and the corresponding characteristic vector is $(0,1)^{\text{T}}$. When the system is on the exceptional surface, the response of the system will be directly determined by ω_0. The loss Γ, the coupling rate κ and the phase difference θ_1 and θ_2 cannot make the system break away from the exceptional surface, this means that factors independent of the frequency perturbation ε_ω and the zero response of the system will form a zero-valued surface consisting of several exceptional points. This is also a manifestation of its robustness; that is, it does not deviate from the exceptional point like an isolated EP system when disturbed by irrelevant factors, as shown in Fig. 3.

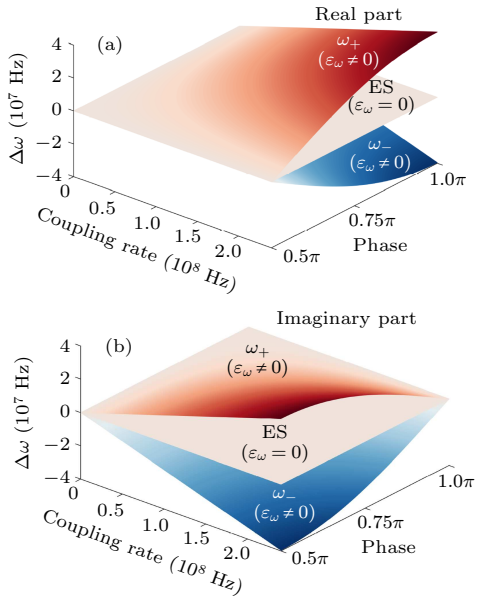


Fig. 3. The response of the system when the frequency perturbation is 0 versus not 0. (a) The real part of the response. (b) The imaginary part of the response. The upper and lower surfaces correspond to a rotational speed of 0.5 rad/s. In the figure we use the parameters $r_{\text{R}} = 0.714$, $\theta_1 = \theta_2 = \pi$, $\alpha = 0.98$. The FC power separation ratio in both the left and right fiber loop mirrors is 85:15. The power separation ratio of FC(1×2) is 50:50. The area of the resonator RS is 0.0225 m^2 and the area of the resonator X is 0.011166 m^2.

When the system is perturbed by frequency, it will have a completely different response than other unrelated perturbations. When the system is subjected to the frequency perturbation caused by rotation, the effect of the perturbation on the system can be expressed by the perturbation Hamiltonian matrix

$$H_{\varepsilon_\omega} = \begin{bmatrix} \varepsilon_\omega & \kappa r_{\text{L}}(\varepsilon_\omega)\mathrm{e}^{2\mathrm{i}\theta_1} \\ 0 & -\varepsilon_\omega \end{bmatrix}. \tag{9}$$

So, the Hamiltonian matrix of the whole system is $H_{\text{ES}} + H_{\varepsilon_\omega}$, and the eigenfrequency is obtained by solving the problem

$$\omega_\pm = \omega_0 - \mathrm{i}\Gamma \pm \sqrt{\kappa_1\kappa_2 + \varepsilon_\omega^2}, \tag{10}$$

$$\Delta\omega_\pm = \pm\sqrt{\kappa_1\kappa_2 + \varepsilon_\omega^2}, \tag{11}$$

where $\kappa_1 = r_{\text{L}}(\varepsilon_\omega)\mathrm{e}^{2\mathrm{i}\theta_1}\kappa$, $\kappa_2 = r_{\text{R}}\mathrm{e}^{2\mathrm{i}\theta_2}\kappa$, and ε_ω^2 can be ignored at smaller rotations, so the splitting distance ΔF can be expressed as

$$\Delta F = \omega_+ - \omega_- \approx 2\sqrt{r_{\text{L}}(\varepsilon_\omega) r_{\text{R}}\mathrm{e}^{2\mathrm{i}(\theta_1+\theta_2)}\kappa^2}. \tag{12}$$

The system responses at different coupling rates are shown in Fig. 4, where the real part represents the frequency split and the imaginary part represents the corresponding broadening.

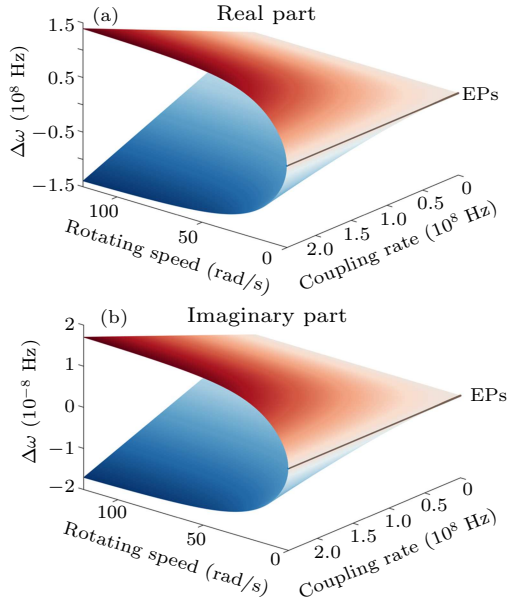


Fig. 4. Curves of $\omega_\pm$ versus angular rate for different coupling rates. (a) The real part of the response. (b) The imaginary part of the response. In the figure we use the parameters $r_{\text{R}} = 0.714$, $\theta_1 = \theta_2 = \pi$, $\alpha = 0.98$. The FC power separation ratio in both the left and right fiber loop mirrors is 85:15. The power separation ratio of FC(1×2) is 50:50. The area of the resonator RS is 0.0225 m^2 and the area of the resonator X is 0.011166 m^2.

3. System response and parameters

In this section we will show the response and parameters of the system. To understand the characteristics of the system, we need to obtain the transfer function of the system. According to our system structure, we can get the relationship

between the output port and input port, CW mode, and CCW mode

$$a_{\text{out}} = t_{\text{R}}\left(a_{\text{in}}\,\mathrm{e}^{\mathrm{i}(\theta_1+\theta_2)} + \sqrt{\kappa}a_{\text{CW}}\,\mathrm{e}^{\mathrm{i}\theta_2} + \sqrt{\kappa}r_{\text{L}}a_{\text{CCW}}\,\mathrm{e}^{\mathrm{i}(2\theta_1+\theta_2)} + a_{\text{in}}r_{\text{R}}r_{\text{L}}\,\mathrm{e}^{\mathrm{i}(3\theta_1+3\theta_2)}\right). \quad (13)$$

The relationship between a_{out} and a_{in} can be obtained by combining this equation with coupled mode equations, and then the transfer function can be expressed as $T = |a_{\text{out}}/a_{\text{in}}|^2$. The normalized transmission spectrum is then plotted as shown in Fig. 5(a). The nonlinear response of the system to the rotating angular rate can be clearly seen. As a comparison, the 100 times response of a conventional resonant gyro of the same size is also given. The angular rate sensing enhancement based on the exceptional surface is more prominent at low speed. At the same time, analyzing the transmission spectrum waveform, we can observe that at lower rotational speeds, as the angular rate increases, the trajectory reflects nonlinearity and its full width at half maximum (FWHM) also has a similar trend. This is consistent with the behaviors of the real and imaginary parts of the characteristic frequency.

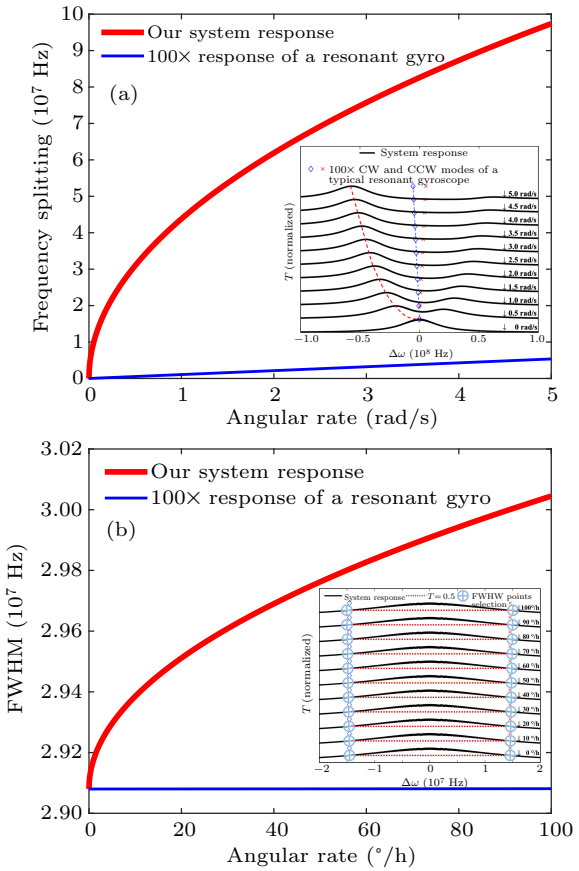


Fig. 5. Comparison of the system transfer function curves at low rotational speeds with 100 times the response of a conventional resonant gyro under the same conditions. (a) Frequency splitting of the system at conventional angular rates. (b) FWHM variation of the system at very low angular rates. In the figure we use the parameters $r_{\text{R}} = 0.714$, $\theta_1 = \theta_2 = \pi$, $\alpha = 0.98$, resonator RS loss $\Gamma = 1.55 \times 10^7$, the coupler coupling rate $\kappa = 2.4 \times 10^8$ and reference frequency $\omega_0 = 193.54839$ THz (corresponding to the wavelength of 1550 nm). The FC power separation ratio in both the left and right fiber loop mirrors is 85:15. The power separation ratio of FC(1×2) is 50:50. The area of the resonator RS is 0.0225 m^2 and the area of the resonator X is 0.011166 m^2.

In particular, when the rotational speed is very small, the splitting distance is extremely weak and much smaller than the mode spread, and the two modes overlap, as shown in Fig. 5(b). As the weaker rotational speed increases slowly, the FWHM of the transmission spectrum increases weakly. When the splitting distance is less than half the FWHM of the modes, the measurement of the frequency splitting changes, and mode splitting measurements will be extremely difficult to carry out under these conditions, and measuring the FWHM of the transmission spectrum will be a better solution. As shown in Fig. 5(b), at very low angular rates, our structure also has a larger response compared to the conventional resonant gyro.

To better observe the whole trends, we plot the transfer function under dense perturbations and normalize it. As shown in Fig. 6, with the left mode more pronounced, the amplitude of the right mode relatively decreases as the rotation speeds up, but it also has the same frequency separation and broadening increasing characteristics as the left mode. The difference between the frequency of the left mode and the frequency of the right mode is used as a subsequent measurement and represents the response of the gyroscope.

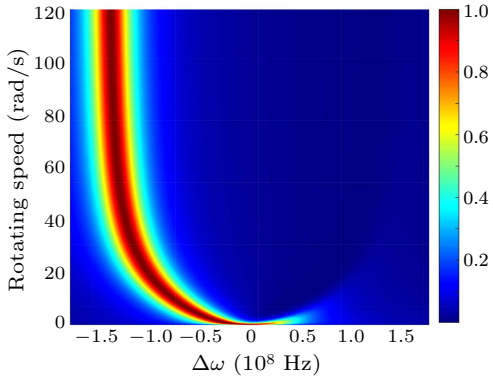


Fig. 6. Top view of the 3D model generated from the variation curves of the system transfer function over a wider range of angular rates. All parameters are the same as in Fig. 5.

By observing the characteristic frequency, we can see that it is related to the sum of the two phases. In our system, a phase shifter is installed next to the right optical loop mirror, which is used to adjust the system to the optimal state. Figure 7 shows the change in system response as the phase modulator passes through a phase cycle when the left phase θ_1 is π. It can be seen that the system will have the best output response when the sum of the two phases is an integer multiple of π. A slight phase shift weakens the system response and increases mode broadening, and the entire system still works normally. But if the sum of the two phases gets too close to the odd times of $\pi/2$, the system response will become very weak, the mode will broaden greatly, and it will hardly work. In the assembly of the system, it is not necessary to measure the specific value of the left phase, but only to traverse the phase modulator through 0–π when the reflectivity of the variable reflectivity device group is not 0, just find the phase in which the system responds the most.

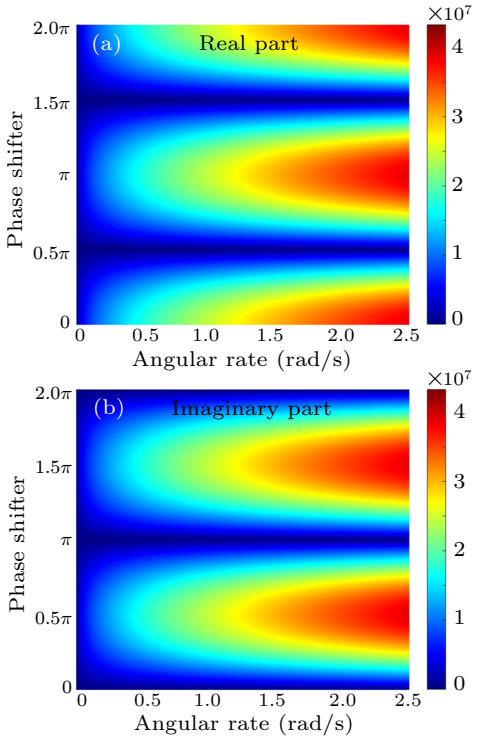


Fig. 7. System response versus angular rate versus phase shifter. (a) The real part of the response. (b) The imaginary part of the response. In the figure we use the parameters $r_R = 0.714$, $\kappa = 2.4 \times 10^8$, $\alpha = 0.98$. The FC power separation ratio in both the left and right fiber loop mirrors is 85:15. The power separation ratio of FC(1×2) is 50:50. The area of the resonator RS is 0.0225 m^2 and the area of the resonator X is 0.011166 m^2.

When we adjust to the appropriate phase, the low-speed sensitivity will be much more than the conventional resonant gyroscope, the system sensitivity calculation method we use is

$$S = \frac{\partial \Delta\omega}{\partial \varepsilon_\omega}. \tag{14}$$

We calculate and derive sensitivity curves using the same parameters, as shown in Fig. 8(a), and compare them with conventional gyroscopes of the same cavity size by looking for two line intersections (XC, YC), we can get (0, XC) optimal rotation rate operating range.

Within this range, the response of the new structure we have designed will be significantly improved compared to conventional gyroscopes. Once it exceeds this range, it will face lower response and nonlinear problems than conventional resonant gyroscopes.

In practical experiments and applications, our system will be affected by noise, making the actual response weaker than the theoretical value. This means that the actual sensitivity enhancement effect decreases and the sensitivity enhancement range shrinks. Since our system is designed as a single-input, single-output structure, the reciprocal and environmental noise will not be able to be canceled out by differential as in a conventional resonant gyro. This causes the resonant frequency point to deviate even before the measurement to be measured is loaded. Also, the actual phase conditions need to be double-checked due to these noise effects. As shown in Fig. 8(b), we simulate the effect of noise on the sensing mechanism by varying the position of the resonant frequency point of the resonator X and changing the phase sum. It can be seen that the optimal operating range of the sensor shrinks to (0,90 rad/s) at an offset of 0.03π of the resonance frequency point and a phase sum offset of 0.04π. Even in this environment the sensitivity at low rotational speeds is still up to 11 times higher than conventional resonant gyros. Although it is difficult to suppress common-mode noise by differential means with this sensor structure, the sensitivity will still be considerable with future multiple closed-loop control.

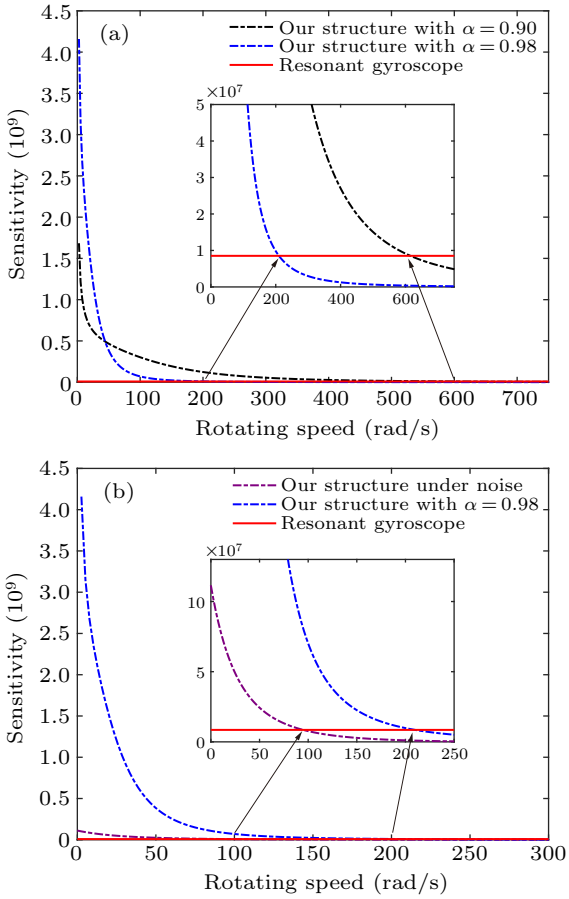


Fig. 8. (a) Sensitivity versus angular rate curves for a system consisting of resonator X with different loss coefficients and as a comparison the sensitivity of a conventional resonant gyro in a straight red line. (b) Comparison of sensitivity when the system is affected by noise and other unfavorable factors. The purple line indicates the change in sensor sensitivity with angular rate as affected by noise or other factors with $\alpha = 0.98$. In the figure we use the parameters $r_R = 0.714$, $\theta_1 = \theta_2 = \pi$ and $\kappa = 2.4 \times 10^8$. The FC power separation ratio in both the left and right fiber loop mirrors is 85:15. The power separation ratio of FC(1×2) is 50:50. The area of the resonator RS is 0.0225 m^2 and the area of the resonator X is 0.011166 m^2. In particular, the parameters of the purple curve in (b) are $\theta_1 = \theta_2 = 1.02\pi$ and the resonant frequency of resonator X deviates from the expected 0.03π.

4. Sensing applications

4.1. Realization of wide working range

Optical gyroscopes often require different working ranges when used in different scenarios, so it is very meaningful to find a way to make the same optical gyroscope have high sensitivity and robustness in as many scenarios as possible. From

a theoretical point of view, we can replace both the resonator RS and the resonator X, but frequent disassembly and assembly are obviously cumbersome, so our structure is achieved by changing the loss coefficient by adjusting the VOA of the resonator X. Since the resonator is required to maintain critical coupling with the fiber coupler, the VRC also needs to be adjusted simultaneously to match the coupling ratio k and the loss coefficient α. This way we avoid rewinding and disassembling the resonator.

For better understanding, the coupled mode equations of a single-cavity reflection resonator are given by

$$b_1 = ta_1 + \mathrm{i}k\alpha \mathrm{e}^{\mathrm{i}\theta} b_2, \tag{15}$$

$$b_2 = \mathrm{i}ka_1 + t\alpha \mathrm{e}^{\mathrm{i}\theta} b_2, \tag{16}$$

where a_1 represents the incident end of the coupler, b_1 represents the transmitting end of the coupler, b_2 represents the coupling end of the coupler, k represents the directional coupling coefficient, t represents the transmission coefficient, $k^2 + t^2 = 1$, θ represents the phase, α represents the loss coefficient, the power separation ratio of 1×2 fiber coupler is 50:50, and r_b is the constant representing the reflectivity of the left loop mirror.

The relationship between reflectivity and phase of the variable reflectivity devices on the left side can be obtained by

$$r_\mathrm{L} = \sqrt{0.5}\left| r_\mathrm{b} \frac{\alpha \mathrm{e}^{\mathrm{i}\theta} - t}{\alpha t \mathrm{e}^{\mathrm{i}\theta} - 1} \right|. \tag{17}$$

To better adapt to other types of optical systems, we set the independent variable as the phase θ, which in our structure is related to the rotation of the sensing fiber ring resonator and the rotation speed

$$\theta = \frac{8\pi A\chi}{c\lambda}, \tag{18}$$

where A is the area enclosed by the fiber ring resonator RS, c is the speed of light, λ is the wavelength, and χ is the rotational angular rate.

The relationship in Fig. 9 between angular rate and reflectivity is given for $\alpha = 0.98$ and $\alpha = 0.90$. The area of the rotating sensing fiber ring resonator is 0.0225 and $r_\mathrm{b} = 0.714$.

It can be clearly seen from Fig. 9 that at the same angular rate, $\alpha = 0.98$ will have a higher reflectivity than $\alpha = 0.90$ reflection structure. To achieve the same reflectivity, $\alpha = 0.90$ requires a higher rotational speed. The sensitivity change rate of the reflection structure with $\alpha = 0.90$ exceeds that of the reflection structure with $\alpha = 0.98$ at around 50 rad/s.

We substitute the reflection structures of the two loss coefficients into the system respectively to derive their sensitivity versus angular rate plots under the same conditions, as shown in Fig. 8(a). We found that its performance in terms of sensitivity is the same as the performance of the sensitivity change rate of the reflection structure. At low speeds, the loss coefficient $\alpha = 0.98$ will achieve higher sensitivity than $\alpha = 0.90$. At high angular rates, the system response sensitivity with loss coefficient $\alpha = 0.98$ decays very quickly. This also means that at high angular rates, the system with $\alpha = 0.90$ performs more prominently. When the loss coefficient is adjusted to $\alpha = 0.90$, the system sensitivity only drops to the sensitivity of the resonant gyroscope at a high speed of about 600 rad/s. Of course, the structure of loading $\alpha = 0.90$ reflection device group significantly sacrifices part of the sensitivity at low speed, but this sensitivity is still much higher than that of the conventional resonant gyroscope. The most suitable loss coefficient can be selected according to the actual situation.

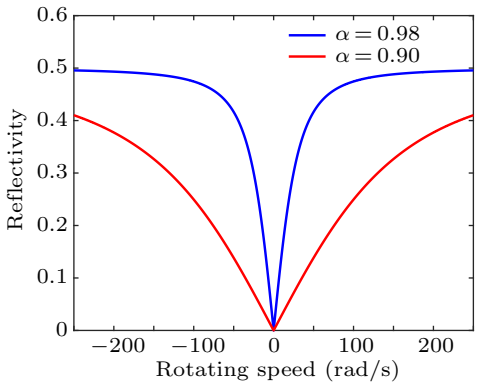


Fig. 9. Variation curves of reflectivity with angular rate at the resonant frequency of the resonator RS of the reflection device consisting of resonator X with different loss coefficients. The FC power separation ratio in both the left and right fiber loop mirrors is 85:15. The power separation ratio of FC(1×2) is 50:50. The area of the resonator RS is 0.0225 m^2 and the area of the resonator X is 0.011166 m^2.

4.2. Determine the direction of rotation

In the previous section, we only studied the angular rate of rotation in one direction. Although it shows great value in improving angular rate sensing, we cannot determine the direction of rotation, which is fatal for an optical gyroscope. In this section, we will analyze the system response to its two-way rotation and demonstrate our angular rate sensor response to be able to determine the direction of rotation without affecting the above performance.

First, we draw the normalized transfer function graph of the system under bidirectional rotation as shown in Fig. 10(a). It is obvious that the plot is symmetrical about the x-axis, which is quite counterintuitive.

So why can the image not be symmetric about the origin like a normal resonator? Returning to the theoretical derivation in Section 2, we can see that on the exceptional surface, when the one-way coupling from the counterclockwise mode to the clockwise mode is blocked, even if the frequency is perturbed by rotation, the system response still does not show a square-root characteristic; but when the frequency perturbation is 0 and the one-way coupling from the counterclockwise mode to the clockwise mode changes uniformly, the system response shows a square-root dependence. Such a comparison shows that our system's push away from the exceptional surface, and even the subsequent sensing, is directly dependent

on the change in unidirectional coupling from counterclockwise to clockwise mode, rather than on the frequency perturbation. It is just that we use this to unidirectionally couple the counterclockwise mode to the clockwise mode, and link the reflectivity to the angular rate of rotation through the additional reflection structures with the angular rate.

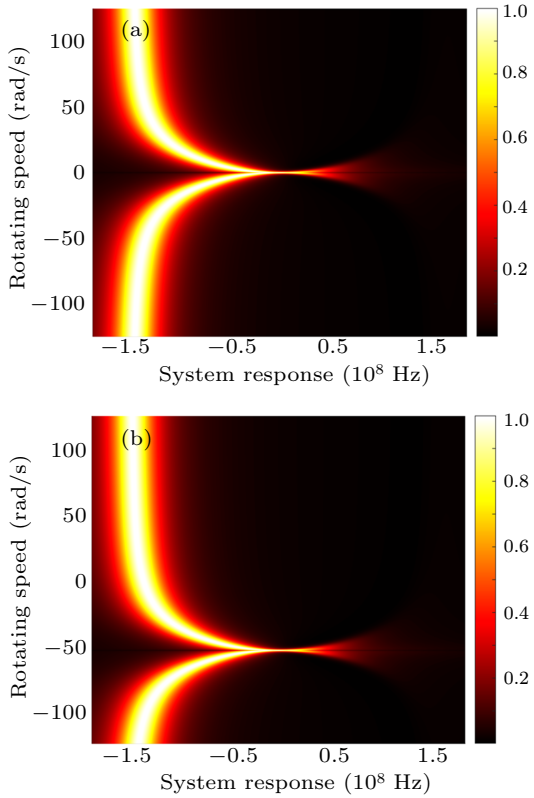


Fig. 10. (a) Schematic representation of the system response as a function of bidirectional angular rate in the vicinity of ω_0. (b) Schematic representation of the system response as a function of bidirectional angular rate in the vicinity of $\omega_0 + \mathrm{FSR_X}$. In the figure we use the parameters $r_\mathrm{R} = 0.714$, $\theta_1 = \theta_2 = \pi$, $\alpha = 0.98$, resonator RS loss $\Gamma = 1.55 \times 10^7$, the coupler coupling rate $\kappa = 2.4 \times 10^8$ and reference frequency $\omega_0 = 193.54839$ THz (corresponding to the wavelength of 1550 nm). The FC power separation ratio in both the left and right fiber loop mirrors is 85:15. The power separation ratio of FC(1×2) is 50:50. The area of the resonator RS is 0.0225 m^2 and the area of the resonator X is 0.011166 m^2.

We observe the blue curve in Fig. 2, which is symmetric in CW rotation and CCW rotation. The x-axis symmetry shown in Fig. 10(a) shows the symmetry of the reflectivity in both CW and CCW rotation.

To distinguish the direction of rotation, we can focus on the next resonant frequency point of the ring resonator X because the area of the fiber ring resonator RS is 2.015 times that of the ring resonator X, the resonant frequency of the fiber ring resonator RS is 0.03π to the previous frequency point of the ring resonator X, and the relationship between the reflectivity and the angular rate is shown by the orange curve in Fig. 2.

Then, we substitute the relationship between reflectivity and rotational angular rate into the transfer function formula, and obtain the sensor response of the next cycle as shown in Fig. 10(b).

It can be seen that the image in Fig. 10(b) seems to be shifted on the rotational speed axis of Fig. 10(a). As shown in Fig. 2 near $\omega_0 + \mathrm{FSR_X}$, the resonant frequencies of the ring resonator X and the ring resonator RS do not coincide. Therefore, when the angular rate is 0, the reflectivity corresponding to its characteristic frequency is not 0, which results in a considerable response of the system near $\omega_0 + \mathrm{FSR_X}$ when it is not rotating. We will use the resulting asymmetry to determine the direction. We use FPGA and MCU to capture the system response near ω_0 and $\omega_0 + \mathrm{FSR_X}$ in real time and convert it to angular rate. When we capture that the angular rate increases from 0, the system response change trend near $\omega_0 + \mathrm{FSR_X}$ will have two possibilities: increase or decrease, corresponding to rotation in two directions respectively.

Since the resonance curve of the ring resonator X is periodic under small wavelength changes, its system responses near ω_0 and $\omega_0 + \mathrm{FSR_X}$ should have the same linear change trend, although they correspond to different angular velocities. We can approximate the sensitivity of this method to determine the direction of rotation by using the sensitivity near 50 rad/s. Its sensitivity is about 30 times that of conventional resonant gyroscopes. When the ring resonator is replaced with $\alpha = 0.90$ in Subsection 4.1, its sensitivity near 50 rad/s will be higher, so our judgement method does not conflict with the fast switching working range in Subsection 4.1.

5. Conclusion and perspectives

We propose a new exceptional surface angular rate sensor structure, which overcomes the disadvantages of conventional resonant gyroscopes that cannot have both sensitivity and volume advantages, and solves the problem that the gyro operating point of an isolated EP is susceptible to external unmeasured disturbances. At the same time, we cleverly make the rotation push the system working point away from the exceptional surface. By analyzing the system's characteristic frequencies and transfer functions, we optimized the parameters. It is concluded that under these parameters, our exceptional surface angular rate sensor has achieved a high sensitivity that is approximately 300 times that of the conventional resonant gyroscope at low speed. Then, we analyzed the resolution of the rotation direction and the adjustment of the working range at the application level, so that the sensitivity can still be better than the conventional resonant gyroscope at a high speed of 600 rad/s. This makes up for the shortcomings of existing similar models that cannot distinguish the direction of rotation and have a small working range. Our new structure provides new ideas for the development of non-Hermitian gyroscopes, making it possible for exceptional surface angular rate sensors to take into account both sensitivity and working range.

Appendix A: Primary experimental evidence

Here we give primary experimental validation results of additional reflection structures and exceptional surface structures, respectively. We perform a simple preliminary verification of the theoretical model through these experiments.

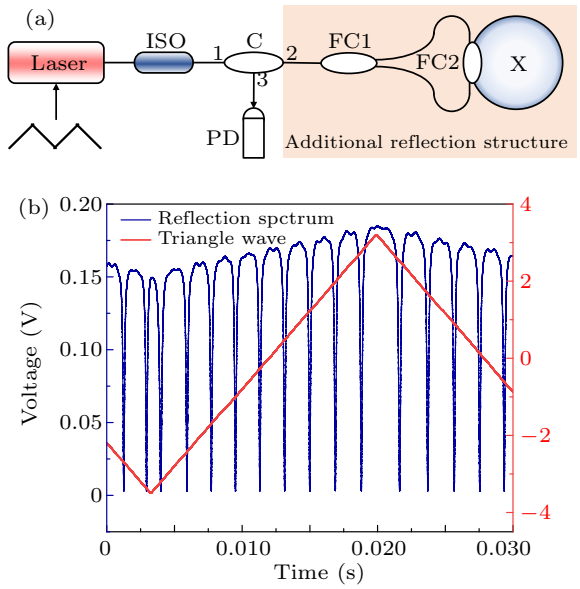


Fig. A1. Experimental validation of additional reflection structure. (a) Schematic diagram of the experimental setup. X: resonator X length 2.2 meters. ISO: isolator. C: circulator. FC1: fiber coupler with 50:50 power separation ratio. FC2: fiber coupler with 80:20 power separation ratio. PD: photodetector. (b) Diagram of the experimental results. The red line is the voltage signal loaded on the laser. Vpp (peak-to-peak voltage): 7 V. Frequency: 30 Hz.

We use a tuneable laser operating mainly in the 1550 nm band. A triangular wave is loaded on the laser through the signal generator output (red curve in Fig. A1(b)), and the output wavelength of the laser varies linearly and periodically under the voltage signal of the triangular wave. By scanning the wavelength in this way, we obtain a curve of the reflected power as a function of time (wavelength), as shown by the blue curve in Fig. A1(b). We can observe that the reflected light intensity obtained at different frequencies exhibits a clear Lorentzian line shape, which is consistent with our theoretical derivation in Section 2. In addition to the requirement that the reflectivity exhibits a Lorentzian line shape with frequency, our theory also requires that the resonator X is in a critically coupled state. We obtained that the resonance depth of the resonator X under the experimental conditions at this time is 99.86% by analyzing the data, which can basically be considered as critically coupled.

Then, we explore the nonlinear response of the exceptional surface. As shown in Fig. A2(a), we built the exceptional surface structure in Section 2 and prompted the response of the exceptional surface structure with the left optical loop mirror. We did a set of control experiments with the light path without adding the left optical loop mirror (left reflectivity 0), the light path with the optical loop mirror with the coupler FC5 added as 99:1 (left reflectivity 0.199), and the light path with the optical loop mirror with the coupler FC6 added as 90:10 (left reflectivity 0.6). Slightly different from Section 3, the resonator RS in our experiment is lossy, which does not affect the preliminary validation results. As shown in Fig. A2(b), we can find that under such phase conditions and resonator conditions, with the increase of unidirectional coupling, a new mode is gradually generated on the left side of the spectral line, which has a very small change in amplitude compared to the mode on the right side. Moreover, the tendency of increasing splitting distance becomes smaller with increasing reflectivity, which verifies the nonlinear response of the exceptional surface and shows that sensitive enhancement can be realized.

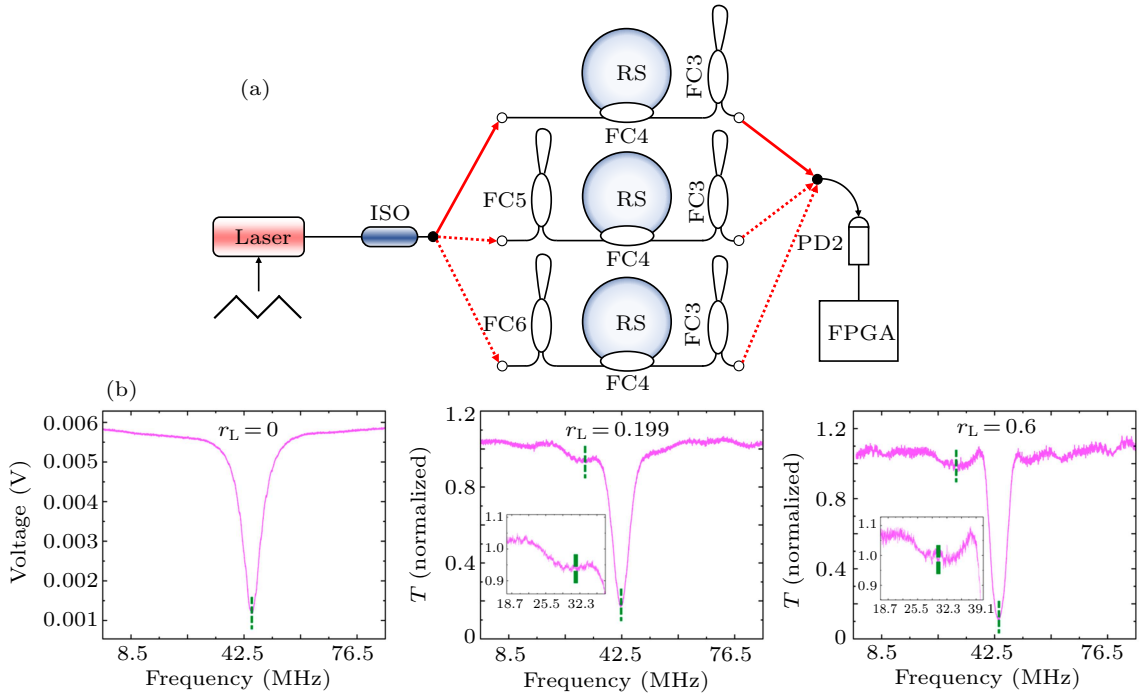


Fig. A2. Experimental validation of the exceptional surface nonlinear response. (a) Schematic of the control experimental setup. ISO: isolator. RS: rotation-sensitive resonator length 2 meters. FC3: fiber coupler with 80:20 power separation ratio. FC4: fiber coupler with 90:10 power separation ratio. FC5: fiber coupler with 99:1 power separation ratio. FC6: fiber coupler with 90:10 power separation ratio. The phase sum between the optical loop mirrors was controlled to be around 1.65π. PD2: photodetector. (b) Experimental results diagrams demodulated from F-P modes with FPGA.

Acknowledgements

Project supported in part by the National Natural Science Foundation of China (Grant Nos. 62273314, U21A20141, and 51821003); Fundamental Research Program of Shanxi Province (Grant No. 202303021224008); and Shanxi Province Key Laboratory of Quantum Sensing and Precision Measurement (Grant No. 201905D121001).

References

[1] Liu S, Hu J, Wang Y, Liu Q, Ma H and He Z 2023 *Opt. Lett.* **48** 1152
[2] Liu H D, Liu W Y, Zhao R, Pan Z W, Ding S X, Tao Y, Zhang W, Zhou Y R, Xing E B, Tang J, Liu J and Chen J J 2023 *Opt. Commun.* **533** 129285
[3] Li H, Ni P, Wang Q, Feng C and Feng L 2021 *Journal of Lightwave Technology* **39** 1858
[4] Wang C, Jiang X, Zhao G, Zhang M, Hsu C W, Peng B, Stone A D, Jiang L and Yang L 2020 *Nat. Phys.* **16** 334
[5] Grant M J and Digonnet M J F 2020 *Opt. Lett.* **45** 6538
[6] Li A, Wei H, Cotrufo M, Chen W, Mann S, Ni X, Xu B, Chen J, Wang J, Fan S, Qiu C W, Alu A and Chen L 2023 *Nat. Nanotechnol.* **18** 706
[7] Lee S B, Yang J, Moon S, Lee S Y, Shim J B, Kim S W, Lee J H and An K 2009 *Phys. Rev. Lett.* **103** 134101
[8] Wiersig J 2016 *Phys. Rev. A* **93** 033809
[9] Katsantonis I, Droulias S, Soukoulis C M, Economou E N, Rakitzis T P and Kafesaki M 2022 *Phys. Rev. B* **105** 174112
[10] Xing T, Pan Z, Tao Y, Xing G, Wang R, Liu W, Xing E, Rong J, Tang J and Liu J 2020 *J. Phys. D Appl. Phys.* **53** 205102
[11] Wang K, Xiao L, Lin H, Yi W, Bergholtz E J and Xue P 2023 *Sci. Adv.* **9** eadi0732
[12] Zhong Q, Kou J, Ozdemir S K and El-Ganainy R 2020 *Phys. Rev. Lett.* **125** 203602
[13] Zhang H, Li W, Han P, Chang X, Liu J, Huang A and Xiao Z 2019 *J. Appl. Phys.* **125** 084502
[14] De Carlo M, De Leonardis F, Lamberti L and Passaro V M N 2019 *Opt. Lett.* **44** 3956
[15] Chen T, Xiao Z, Jiang S, Li W, Li J, Wang Y, Wang X, Huang A and Zhang H 2022 *J. Appl. Phys.* **131** 243101
[16] Yang F, Liu Y C and You L 2017 *Phys. Rev. A* **96** 053845
[17] Zhang H, Peng M, Xu X W and Jing H 2022 *Chin. Phys. B* **31** 014215
[18] Li W, Zhang H, Han P, Chang X, Jiang S, Zhou Y, Huang A and Xiao Z 2020 *J. Appl. Phys.* **128** 134503
[19] Lai Y H, Suh M G, Lu Y K, Shen B, Yang Q F, Wang H, Li J, Lee S H, Yang K Y and Vahala K 2020 *Nat. Photon.* **14** 345
[20] Lai Y H, Lu Y K, Suh M G, Yuan Z and Vahala K 2019 *Nature* **576** 65
[21] Khial P P, White A D and Hajimiri A 2018 *Nat. Photon.* **12** 671
[22] Jiang S, Chang X, Li W, Han P, Zhou Y, Zhang H, Huang A and Xiao Z 2019 *J. Opt. Soc. Am. B Opt. Phys.* **36** 2618
[23] Wiersig J 2022 *Phys. Rev. A* **106** 063526
[24] Zhong Q, Ren J, Khajavikhan M, Christodoulides D N, Ozdemir S K and El-Ganainy R 2019 *Phys. Rev. Lett.* **122** 153902
[25] Qin G Q, Xie R R, Zhang H, Hu Y Q, Wang M, Li G Q, Xu H, Lei F, Ruan D and Long G L 2021 *Laser & Photonics Reviews* **15** 2000569
[26] Soleymani S, Zhong Q, Mokim M, Rotter S, El-Ganainy R and Ozdemir S K 2022 *Nat. Commun.* **13** 599
[27] Yang H, Mao X, Qin G Q, Wang M, Zhang H, Ruan D and Long G L 2021 *Opt. Lett.* **46** 4025
[28] Li W, Zhou Y, Han P, Chang X, Jiang S, Huang A, Zhang H and Xiao Z 2021 *Phys. Rev. A* **104** 033505
[29] Doran N J and Wood D 1988 *Opt. Lett.* **13** 56
[30] Mortimore D B 1988 *Journal of Lightwave Technology* **6** 1217